

Development of a novel 10-echo multi-contrast sequence based on EPIK to deliver simultaneous quantification of T_2 and T_2^* with application to oxygen extraction fraction

Fabian Küppers^{1,2}  | Seong Dae Yun¹  | N. Jon Shah^{1,3,4,5} 

¹Institute of Neuroscience and Medicine 4, INM-4, Forschungszentrum Jülich, Jülich, Germany

²RWTH Aachen University, Aachen, Germany

³Institute of Neuroscience and Medicine 11, INM-11, JARA, Forschungszentrum Jülich, Jülich, Germany

⁴JARA - BRAIN - Translational Medicine, Aachen, Germany

⁵Department of Neurology, RWTH Aachen University, Aachen, Germany

Correspondence

N. Jon Shah, Institute of Neuroscience and Medicine 4, INM-4, Forschungszentrum Jülich, 52428 Jülich, Germany.
Email: n.j.shah@fz-juelich.de

Purpose: The simultaneous quantification of T_2 and T_2^* maps based on fast sequences for combined GE and SE acquisition has rekindled research and clinical interest by offering a wide range of attractive applications, e.g., dynamic tracking of oxygen extraction fraction (OEF). However, previously published methods based on EPI-readouts have been hindered by resolution and the number of acquired echoes.

Methods: This work presents a novel 10-echo GE-SE EPIK (EPI with keyhole) sequence for the rapid quantification of T_2 . T_2/T_2^* maps from the GE-SE EPIK sequence were validated using three phantoms and 15 volunteers at 3T. The incorporation of a sliding window approach, combined with the full sampling of the k-space center inherent to EPIK, enables a high effective temporal resolution. That is, for an eight-slice breath-hold experiment, a temporal sampling rate of eight reconstructed slices per 1.1 s.

Results: In comparison with repeated single-echo SE, multi-echo GE, and spectroscopy methods, the GE-SE EPIK sequence shows good agreement in quantifying T_2/T_2^* values, while the gray matter/white matter separation yielded the expected contrast differentiation. The OEF was calculated with a view to an initial application with clinical relevance, producing results comparable to those in the literature and with good sensitivity in breath-hold experiments.

Conclusions: GE-SE EPIK provides increased resolution and more echoes, including two SEs, than comparable sequences. Moreover, GE-SE EPIK achieves this within an acquisition time of 57 s for 20 slices (matrix size = 128×128; FOV = 24 cm) and with a reasonably short TE for the final echo (114 ms). The sequence can dynamically track OEF changes in a breath-hold experiment.

KEYWORDS

EPI with keyhole, gradient echo/spin echo, multi-contrast, oxygen extraction fraction, quantitative mapping

1 | INTRODUCTION

The combined acquisition of gradient echo (GE) and spin echo (SE) data offers potential benefits in a wide range of applications and is also advantageous in perfusion and fMRI studies, where it can be used to calculate cerebral blood volume (CBV), cerebral blood flow (CBF), and oxygen extraction fraction (OEF), potentially aiding the interpretation of various pathological and physiological effects. This is particularly relevant in the investigation of tumor heterogeneity, for example, brain tumors¹. Furthermore, dynamic susceptibility contrast (DSC) MRI also benefits from the simultaneous acquisition of GE and SE data² as it allows the different sensitivities of GE and SE to the vessel size to be exploited³.

It has been shown that T_2' , rapidly accessed via simultaneous T_2 and T_2^* acquisition, is directly related to OEF⁴. OEF is a particularly useful parameter for the characterization of brain metabolism and physiology in different brain states, such as a loss of cerebral perfusion pressure⁵, for the prediction of subsequent stroke occurrence in patients with cerebrovascular disease³ and to reflect the perfusion state in acute ischemic stroke^{6,7}. Moreover, combining OEF with CBF data can provide access to the cerebral metabolic rate of oxygen consumption ($CMRO_2$), giving insight into the energy consumption of neuronal activities⁸. As the current gold standard for OEF is O_{15} -PET, an invasive measurement using radioactive isotopes, alternative MRI-based methods for OEF computation are very attractive. As such, the application to OEF is the focus of this manuscript.

The versatility of combined GE and SE methodology has been demonstrated in various approaches, based on a wide range of sequence implementations, and differing in the readout (single- or multiple-line acquisition), spatial resolution, number and type of echoes used. Further details relating to the most relevant of these studies can be found in Supporting Information Appendix S1.1, which is available online.

EPI outperforms single-line acquisitions in terms of acquisition time (TA) and temporal resolution, making it the current method of choice for fast imaging sequences. The matrix size used in such approaches is usually around 64×64 up to 96×96 , whereby most sequences are based on five-echo implementations. Although two implementations^{9,10} provided higher resolutions ($128 \times 128 / 220 \times 220$), they suffered from a small number of echoes (two/five), as well as relatively large TE of the SE (98/138 ms).

With the exception of MASAGE-IEPI¹¹, to date, no other EPI-based sequence acquires a second SE. MASAGE-IEPI takes advantage of small SE TEs as they

dispose with initial GE data to directly apply the refocusing pulse after excitation. However, MASAGE-IEPI has a low spatial resolution based on a matrix size of 64×64 , and it was only applied on animal scanners. Conversely, EPI readouts in multi-echo implementations often lead to long echo-times for late echoes (e.g., 130–150 ms), resulting in a loss of SNR and a long TR, which in turn reduces the number of slices that can be covered in a given TR. To overcome these limitations, Shah et al. proposed EPIK (EPI with keyhole)^{12,13}, which was validated at 1.5T/3T^{14,15}.

To exploit EPIK, this work details the further development of five-echo GE-SE EPIK to acquire 10 GESE echoes (i.e., 2 GEs, 6 with mixed GESE contrast, and 2 SEs) for the simultaneous quantification of T_2 and T_2^* . It is shown that the novel 10-echo GE-SE EPIK sequence outperforms previously published sequences regarding resolution and the number and timing of echoes. The first echoes provide a comparable or even shorter TE than sequences in the literature and, at the same time, the sequence is expanded with additional echoes with higher resolution. The resulting 10-echo sequence includes a second SE for enhanced contrast information and is based on a matrix size of 128×128 yielding a nominal spatial resolution of $1.9 \times 1.9 \text{ mm}^2$. It enables acquisitions with greater brain coverage and with acceptable TE ranges ($< 114 \text{ ms}$) at 3T, especially for the early echoes.

Compared to standard single-shot EPI with the same spatial resolution, a major advantage of EPIK is the higher effective temporal resolution because of a unique keyhole and data sharing in peripheral k-space. In contrast to multi-shot EPI, EPIK ensures a more robust acquisition of temporal signals by sampling central k-space, including the zero line of k-space, in each shot. That is, shot-to-shot instabilities are significantly reduced in EPIK compared to multi-shot EPI^{16,17}. Nevertheless, note that the sliding window technique can also be employed in multi-shot EPI. Additionally, unlike multi-shot EPI, EPIK samples a center of k-space in each shot, i.e., a major fraction of the k-space energy. The strength of the proposed method is in measuring the dynamic time course of relaxation times and OEF. The dynamic nature of such measurements has been shown to provide information of potential clinical interest; DSC methods make use of a dynamic T_2/T_2^* time course to characterize blood flow and volume¹⁸. On the other hand, repeatedly measured OEF¹⁹ is useful for studying dynamic processes in brain activation.

GE-SE EPIK was verified at 3T by comparing T_2 and T_2^* maps from phantom and in vivo data to those from reference methods. Moreover, as an initial proof-of-principle application to dynamically track an OEF time course after a modulation, GE-SE EPIK was applied in a breath-hold experiment.

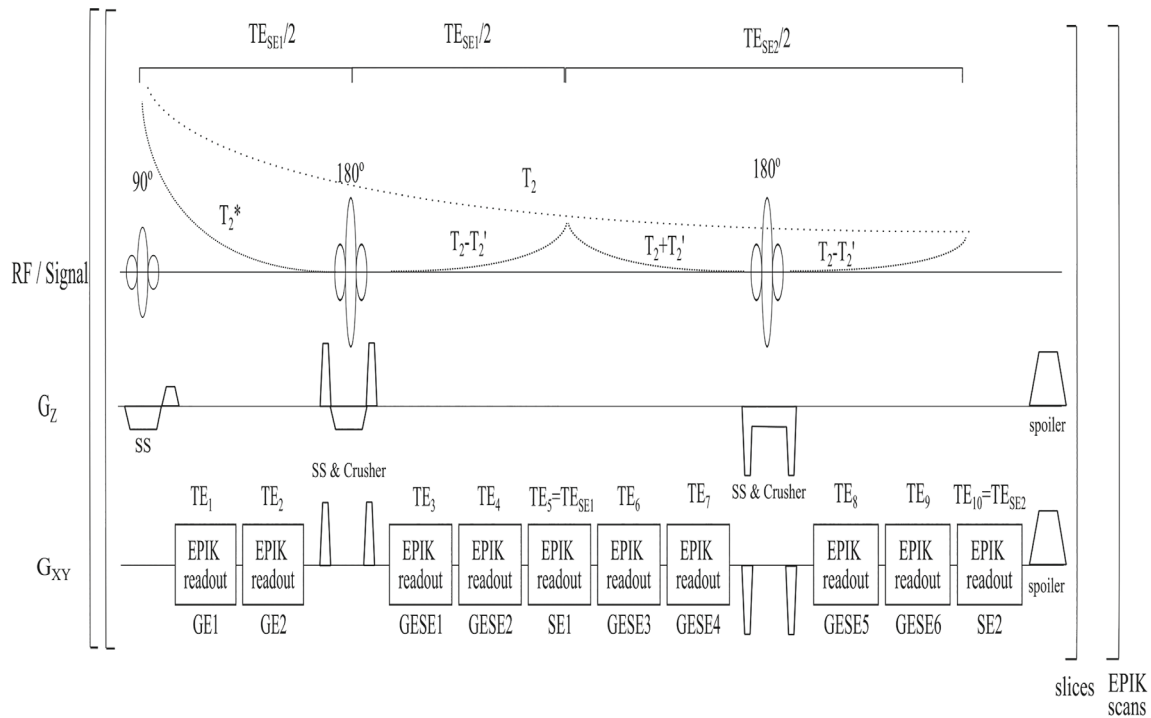


FIGURE 1 Sequence diagram of 10-echo GE-SE EPIK with signal decay and timing declarations. A fat suppression module is applied before each excitation. After each excitation pulse, three non-phase-encoded navigator echoes are acquired to correct for a possible mismatch between even and odd lines. At the end of each excitation, crusher gradients are applied on all three gradient axis. Three preparatory scans are used to reach a steady-state before each measurement. The acquisition of EPIK was configured with 14-shot sampling for the peripheral k-space and full sampling for the central 16 k-space lines. A GRAPPA factor of two for image acceleration was used. Thus, each EPIK readout consists of 12 k-space encoding lines for a final matrix size of 128×128 . The removal of unwanted signal paths from STEs was guaranteed by a pair of crusher gradients around each refocusing pulse⁴⁹

2 | METHODS

2.1 | Sequence implementation

Figure 1 presents the 10-echo GE-SE EPIK sequence, including the expected signal decay and timings. All EPIK readouts were implemented with a matrix size of 128×128 , giving a nominal resolution of $1.9 \times 1.9 \times 3 \text{ mm}^3$ for a FOV of $24 \times 24 \text{ cm}^2$. An EPIK multi-shot factor of 14 with 16 keyhole lines and a GRAPPA²⁰ factor of two was used. The k-space data reconstruction was based on a sliding window technique to ensure that the k-space line-sharing for sparse regions from consecutive data sets is continuously updated. The achievable TEs with corresponding echo types were as follows: 10(GE)/20(GE)/37(GESE)/47(GESE)/57(SE)/67(GESE)/77(GESE)/94(GESE)/104(GESE)/114(SE) ms. Further details are given in the figure caption. As the previously published GE-SE sequences based on EPI readouts mostly had a matrix size of 96×96 with one pure SE, we also implemented our 10-echo approach using a matrix size of 96×96 , leading to an in-plane resolution of $2.5 \times 2.5 \times 3 \text{ mm}^3$.

Further details on the sequence parameters are included in the Appendix S1.2.

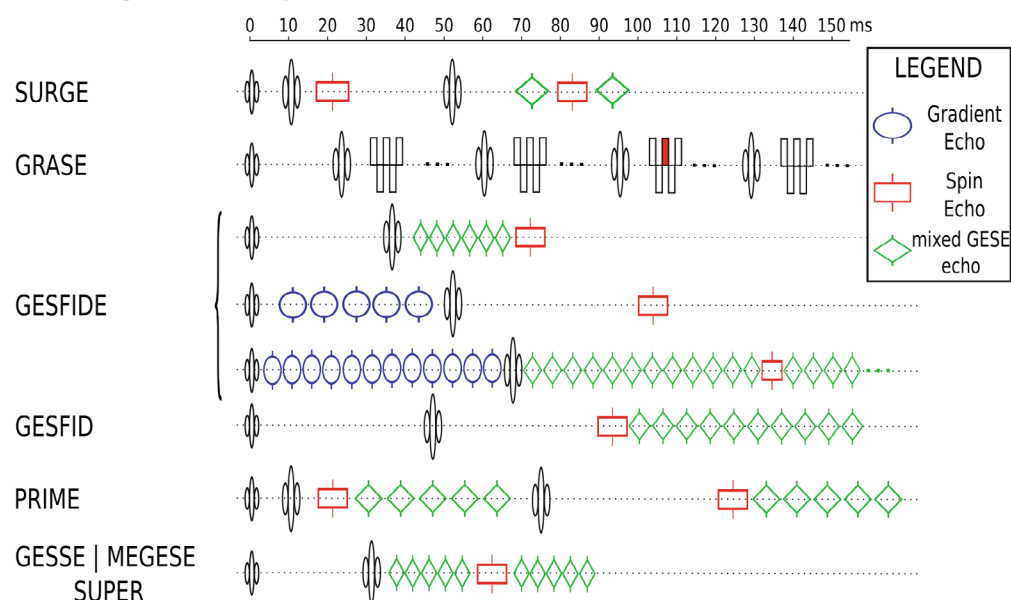
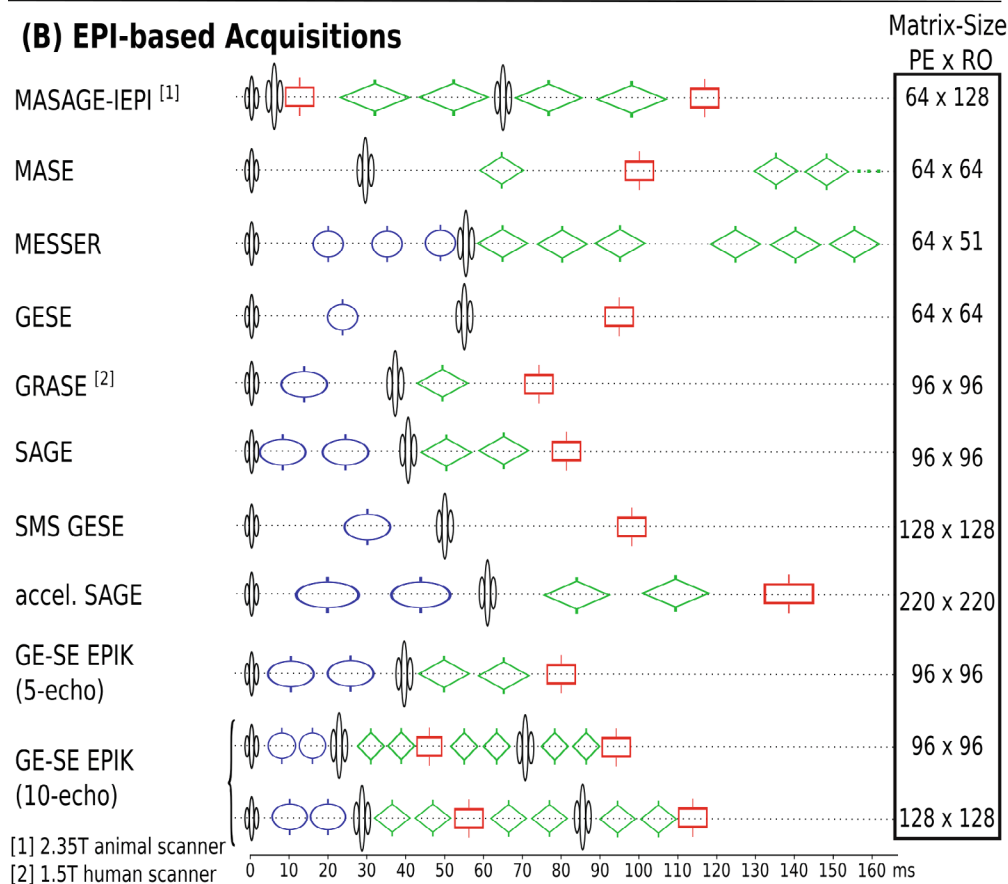
All measurements were performed using a 3T PRISMA (Siemens, Erlangen, Germany) with a 20-channel receiver coil; the body coil was used for transmission.

2.2 | Sequence comparison

Figure 2 shows a comparison of the previously published sequences based on the simultaneous acquisition of GE and SE with two EPIK variants. The time scale on the horizontal axis aids identification of the type and timing of the implemented echoes. Here, 10-echo GE-SE EPIK is compared with EPI-based readout methods. The matrix sizes reported in the previous literature are generally 96×96 and 220×220 at maximum. This 220×220 sequence⁹ only acquired one pure SE at a FOV of 220 mm and a TA of 4 min. Conversely, our method is shown to be superior in terms of the combination of matrix size and the number of echoes and their TEs, i.e., 10 echoes, including two pure SEs, can be acquired with a matrix size of 128×128 .

FIGURE 2

Comparison of published sequence timing and echo generation for the combined GE-SE sequences. The sequences are arranged by the method of k-space sampling: single-line acquisition (A) or EPI-based readouts (B). The horizontal axis shows the type and timing of the implemented echoes on a time scale in milliseconds

(A) Single-line Acquisitions**(B) EPI-based Acquisitions**

Both the 96×96 and 128×128 matrix sizes offer the highest number of echoes compared to previous sequences and have the shortest TE for the first SE of all the published EPI-based sequences that contain at least one initial pure GE.

2.3 | Phantom acquisition

Three single-compartment spherical phantoms were produced as described in the Appendix S1.3. Phantom measurements were conducted with four slices at a resolution

of $1.9 \times 1.9 \times 3 \text{ mm}^3$ and with an in-plane FOV of $24 \times 24 \text{ cm}^2$. Reference acquisitions for T_2^* were performed with a multi-echo (64) gradient-echo sequence (mGE)²¹ employing bipolar readout. The employed TEs ranged from 2.90 to 89.94 ms, with echo spacing of 1.38 ms and $\text{TR} = 1200 \text{ ms}$ with flip angle (FA) = 75° . Reference T_2 maps were calculated using four measurements from a single-echo SE sequence (sSE), obtained at TEs of 10/35/60/85 ms, respectively, with $\text{TR} = 4500 \text{ ms}$, FA = 90° and a 180° refocusing pulse for every SE. GE-SE EPIK with a matrix size of 128×128 was applied with the above-mentioned settings and $\text{TR} = 1000 \text{ ms}$ and FA = 90° .

Spectroscopy measurements based on a single-voxel spin-echo sequence were performed. Each spectroscopy measurement consisted of 50 averages with $\text{TR} = 5 \text{ s}$. Six TEs were acquired for each phantom: from 30 ms with equal steps to twice the expected T_2 range (80/100/180 ms for the respective three phantoms). For each phantom, four different volumes of interest ($10 \times 10 \times 10 / 20 \times 20 \times 20 / 30 \times 30 \times 30 / 40 \times 40 \text{ mm}^3$), placed in the phantom center, were acquired.

2.4 | In vivo acquisition

Fifteen healthy volunteers (25–52 y, six females) were recruited for this study. Written informed consent was obtained from each participant prior to the study. Ethical approval (226/09) was covered by the local ethics committee.

The acquisition protocol acquired GE-SE EPIK, mGE and repeated sSE sequences with the same settings as for the phantom measurement but with 20 slices and the following TR: GE-SE-EPIK = 2800 ms / mGE = 2000 ms/sSE = 4500 ms. This led to TA of 57 s, 4:36 min and four times 7:18 min, respectively.

To compare GE-SE EPIK images for the two spatial resolutions, a male volunteer was measured with a protocol consisting of GE-SE EPIK sequences with a matrix size of 96×96 and 128×128 , each with the same number of slices²⁰ and TR (2800 ms) as above.

Breath-hold experiments were performed on three healthy volunteers, acquiring GE-SE EPIK data in six consecutive blocks, each consisting of 50 repetitions, leading to a TA = 60 s for eight slices with $\text{TR} = 1100 \text{ ms}$ and a FA = 75° . The volunteers were instructed to breathe during the first block of 1 min, followed by 1 min of breath-holding on inspiration; this procedure was repeated twice more.

2.5 | Fitting

To obtain relaxation time maps, the following analysis was performed on the images reconstructed from the acquired data.

The T_2 and T_2^* maps from the GE-SE EPIK sequence were calculated by using a non-linear least-squares algorithm (NLSQ) to the following MR signal equation:

$$S(t) = \begin{cases} S_0 \cdot e^{-t/R_2^*} & \text{for } 0 < t < \text{TE}_{\text{SE1}}/2 \\ \frac{S_0}{\delta} \cdot e^{-\text{TE}_{\text{SE1}}(R_2^* - R_2)} \cdot e^{-t(2R_2 - R_2^*)} & \text{for } \text{TE}_{\text{SE1}}/2 < t \leq \text{TE}_{\text{SE1}} \\ \frac{S_0}{\delta} \cdot e^{+\text{TE}_{\text{SE1}}(R_2^* - R_2)} \cdot e^{-tR_2^*} & \text{for } \text{TE}_{\text{SE1}} < t < \frac{1}{2} \cdot (\text{TE}_{\text{SE1}} + \text{TE}_{\text{SE2}}) \\ \frac{S_0}{\Delta} \cdot e^{-\text{TE}_{\text{SE2}}(R_2^* - R_2)} \cdot e^{-t(2R_2 - R_2^*)} & \text{for } \frac{1}{2} \cdot (\text{TE}_{\text{SE1}} + \text{TE}_{\text{SE2}}) < t \leq \text{TE}_{\text{SE2}} \end{cases} \quad (1)$$

Here, TE_{SE1} and TE_{SE2} are the TEs of both spin echoes, respectively. R_2 and R_2^* are the relaxation rates, which are inversely related to the TRs T_2 and T_2^* . δ and Δ are additional fitting parameters intended to correct for the effect of imperfect refocusing pulses. The mean values of δ and Δ obtained for phantom data were 1.10 and 1.16, respectively, whereas the mean values for in vivo data were found to be 1.08 and 1.09, respectively.

The NLSQ approach can provide map quantifications of a single slice in below 30 s on a standard laptop (32 GB RAM; Core i7 4600 M CPU @2.90 GHz, Intel, USA).

Maps obtained from the reference methods were fitted with a non-linear least-squares algorithm, assuming the signal relation given in Equation (2):

$$S(t) = S_0 \cdot \exp(-t/T_2) S(t) = S_0 \cdot \exp(-t/T_2^*) \quad (2)$$

Fat and skull were excluded by using software developed in-house to set a manual threshold on the original GE-SE EPIK image at TE = 10 ms. The largest connected cluster of voxels with non-zero values was then chosen as the ROI.

To aid gray matter (GM) and white matter (WM) ROI analysis, the images from the reference acquisitions were co-registered with SPM12 to GE-SE EPIK. Subsequently, segmentation for WM and GM masks was performed as follows. Brain masks were computed with the help of the brain tissue probability maps obtained from a standard SPM algorithm applied to the SE reference image at TE = 10 ms. Probability thresholds of 0.9 for GM and 0.98 for WM were used. For the GM mask, a further condition was applied to excluded voxels with reduced T_2 due to partial volume effects: a cutoff at the mean whole-brain T_2 value such that only voxels with a T_2 value larger than the mean T_2 of the whole-brain region in both GE-SE EPIK and reference maps were considered.

2.6 | Spectroscopy

Spectroscopy data were Fourier transformed and frequency shifted to extract the frequency peak area as a function of TE. A mono-exponential fit for T_2 was applied, and the four different volume of interest measurements were averaged for a final T_2 . Additionally, an exponential fit for T_2^* was applied directly to the FID of each single TE data of the $10 \times 10 \times 10 \text{ mm}^3$ volume of interest. The smallest voxel size was chosen for the T_2^* measurement to reduce the influence of the more pronounced dephasing across larger voxels, which would compromise the T_2^* results. The final T_2^* was averaged from the six acquired TEs. The minimum mean square error (MMSE) was calculated from the standard deviations from the single fits for both relaxation times.

2.7 | Oxygen extraction fraction

Putative OEF maps are directly dependent on the relaxation rate $R_2'^{22}$:

$$\text{OEF} = \frac{R_2'}{\lambda \cdot 4/3 \cdot \pi \cdot \gamma \cdot \Delta\chi_0 \cdot \text{Hct} \cdot B_0} \quad (3)$$

R_2' can be calculated from R_2 and R_2^* with the help of the relation $R_2' = R_2^* - R_2$ with $R_2 = 1/T_2$. λ is the venous blood volume fraction and is set to 3%²². γ is the gyro-magnetic ratio, while Hct is the fractional hematocrit and is given as the literature value of 0.36. The latter is based on the multiplication of the typical human Hct of 0.42²³ and a tissue to large vessel Hct ratio of 0.85²⁴. B_0 is the main magnetic field strength. The susceptibility difference between the fully oxygenated and deoxygenated blood is given by $\Delta\chi_0$, which has previously been measured to be 0.246 ppm per unit Hct²⁵.

Data from breath-hold experiments were analyzed as described above by fitting T_2/T_2^* to compute a mean OEF value for each slice at each of the 300 time points. To characterize the OEF changes, the slope of the OEF-time envelope was computed by a linear fit, separately for each block.

3 | RESULTS

Figure 3 provides a visual comparison between the 96×96 and 128×128 matrix, showing in vivo T_2 maps derived from GE-SE EPIK based on both matrix sizes. The resolution improvements are particularly visible in the zoomed areas of the image. The following results are all based on the higher resolution GE-SE EPIK implementation with a matrix size of 128×128 .

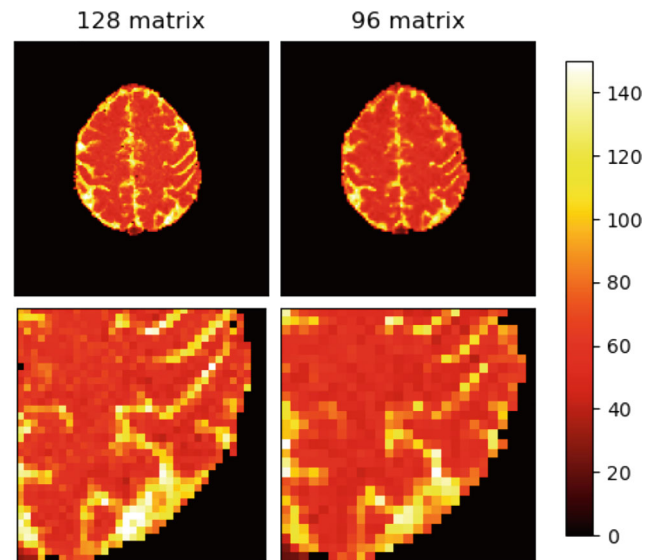


FIGURE 3 Comparison between T_2 maps derived from a GE-SE EPIK sequence based on a 96 matrix size and the novel 128 matrix size implementation. Resolution improvement in the T_2 maps can be clearly seen in the 128 matrix size data

3.1 | Phantom

Phantom results for the carrageenan phantoms are depicted in Figure 4. T_2 and T_2^* maps derived from GE-SE EPIK and the reference methods are shown for one exemplary slice of all three phantoms, including a difference plot on a 20% scale (Figure 4A). A mean value comparison of T_2^* and T_2 between GE-SE EPIK, reference methods and spectroscopy is shown in Figure 4B, while 2D histograms of all acquired phantoms are presented separately for T_2 and T_2^* in Figure 4C. The mean values for each phantom and the relaxation parameter with standard deviation obtained from the GE-SE EPIK method are given as: $T_2(\text{I}) = 44.82 \pm 2.35 \text{ ms}$, $T_2(\text{II}) = 54.12 \pm 3.24 \text{ ms}$, $T_2(\text{III}) = 89.97 \pm 5.19 \text{ ms}$, $T_2^*(\text{I}) = 42.43 \pm 2.97 \text{ ms}$, $T_2^*(\text{II}) = 51.54 \pm 3.95 \text{ ms}$, $T_2^*(\text{III}) = 84.01 \pm 5.24 \text{ ms}$ – where I, II, and III indicate the different phantoms. T_2 results with MMSE from spectroscopy measurements are given as $43.98(0.06)/54.43(0.05)/87.90(0.07) \text{ ms}$, respectively. The corresponding T_2^* results are $41.83(0.04)/52.13(0.05)/83.20(0.10) \text{ ms}$. Both are in good agreement with mean values from the imaging protocol. All values are summarized in Table 1.

3.2 | In vivo

The GE-SE EPIK sequence yielded artifact-free images for all slice locations (Figure 5A) while also depicting the expected contrast evolution through the echo series (Figure 5B). Exemplary T_2 and T_2^* maps derived from

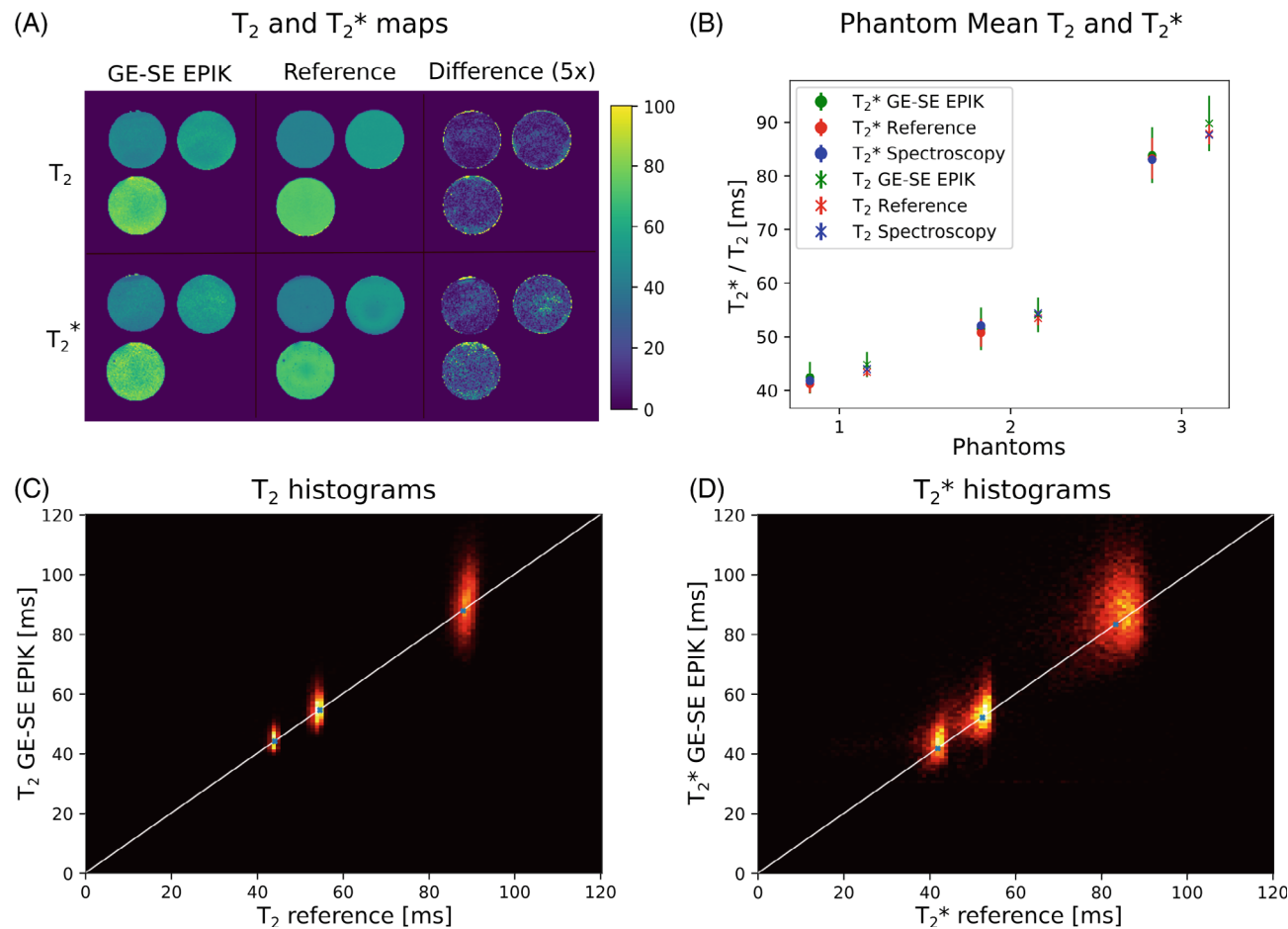


FIGURE 4 Phantom results for three different carrageenan phantoms. The figure provides T₂ and T₂* maps from GE-SE EPIK and a reference method with their differences for all three phantoms (A); a comparison of mean T₂* and T₂ values from GE-SE EPIK, reference methods, and spectroscopy measurements for all three phantoms (B); and a 2D histogram summary for T₂ (C) and T₂* (D) between GE-SE EPIK and the reference methods also including the mean spectroscopy results

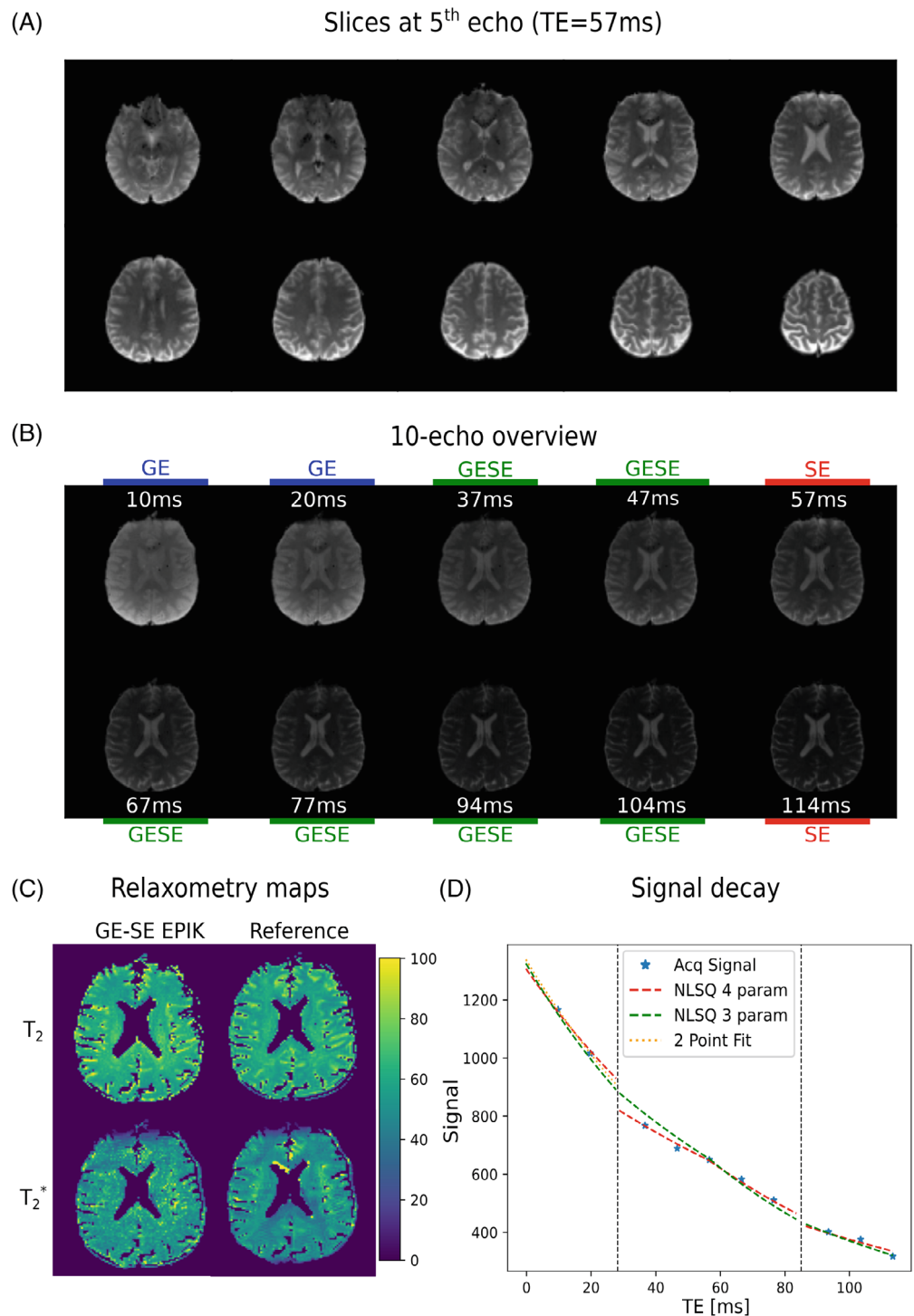
TABLE 1 Summary of mean and SD values for T₂ and T₂* in the whole-brain region as well as for GM and WM ROI derived from the GE-SE EPIK method. Reference results for the whole-brain region and literature values for GM/WM region are given. The second part summarizes T₂* and T₂ values obtained from GE-SE EPIK, reference methods and spectroscopy for three carrageenan phantoms.

Phantom mean (SD)	T ₂ * [ms]			T ₂ [ms]		
	Phantom 1	Phantom 2	Phantom 3	Phantom 1	Phantom 2	Phantom 3
GE-SE EPIK	42.43 (2.97)	51.54 (3.95)	84.01 (5.24)	44.82 (2.35)	54.12 (3.24)	89.97 (5.19)
Reference	41.19 (1.64)	50.80 (2.59)	83.43 (3.80)	43.41 (0.73)	53.51 (1.27)	88.07 (1.99)
Spectroscopy	41.83 (0.04)	52.13 (0.05)	83.20 (0.10)	43.98 (0.06)	54.43 (0.05)	87.90 (0.07)
In vivo mean (Std)	T ₂ * [ms]			T ₂ [ms]		
	Whole brain	WM	GM	Whole brain	WM	GM
GE-SE EPIK	50.14 (9.28)	50.03 (7.23)	55.14 (8.87)	60.53 (7.77)	59.61 (6.06)	67.58 (5.57)
Reference	47.75 (8.91)	47.62 (6.18)	53.92 (8.23)	59.86 (8.22)	58.68 (5.05)	69.45 (6.32)
Literature		50.0 (5.6) ²⁶	55.7 (8.7) ²⁶		62 (4) ²⁷	67 (7) ²⁷

both the GE-SE EPIK method and the reference methods are shown in Figure 5C. A representative single-voxel signal decay is presented in Figure 5D. To underline the

significance of δ , fitting results are also shown with and without its inclusion as an additional fitting parameter. The inclusion of δ yielded a δ value of 1.09.

FIGURE 5 Ten reconstructed slices at the fifth echo ($TE = 57$ ms) obtained from GE-SE EPIK (A), GE-SE EPIK 10-echo overview series (B), T_2/T_2^* maps from GE-SE EPIK and a reference for one exemplary healthy volunteer (C), and the signal intensity decay for a single voxel with the fitting results with and without δ/Δ (D)



To validate the benefits of including 10 echoes in the sequence implementation over fewer echo versions, a comparison of fits using a reduced number of echoes was performed. The in vivo results are depicted in Figure 6, where the different fitting options are shown, including a four-, five-, six-, and eight-echo version; the data were extracted from the fully acquired 10-echo GE-SE EPIK dataset. While the five-echo version only includes a single SE, comparable to the implementation of SAGE or

five-echo GE-SE EPIK, the remaining options account for different numbers of mixed GE-SE echoes. The resulting T_2 distributions clearly demonstrate the benefit of including a second SE as the FWHM improves significantly. In terms of T_2^* , the mean value accuracy is unaffected by the number of fitted echoes, while the FWHM suggests the 8- and 10-echo versions are most precise. The FWHM results are summarized in the figure caption.

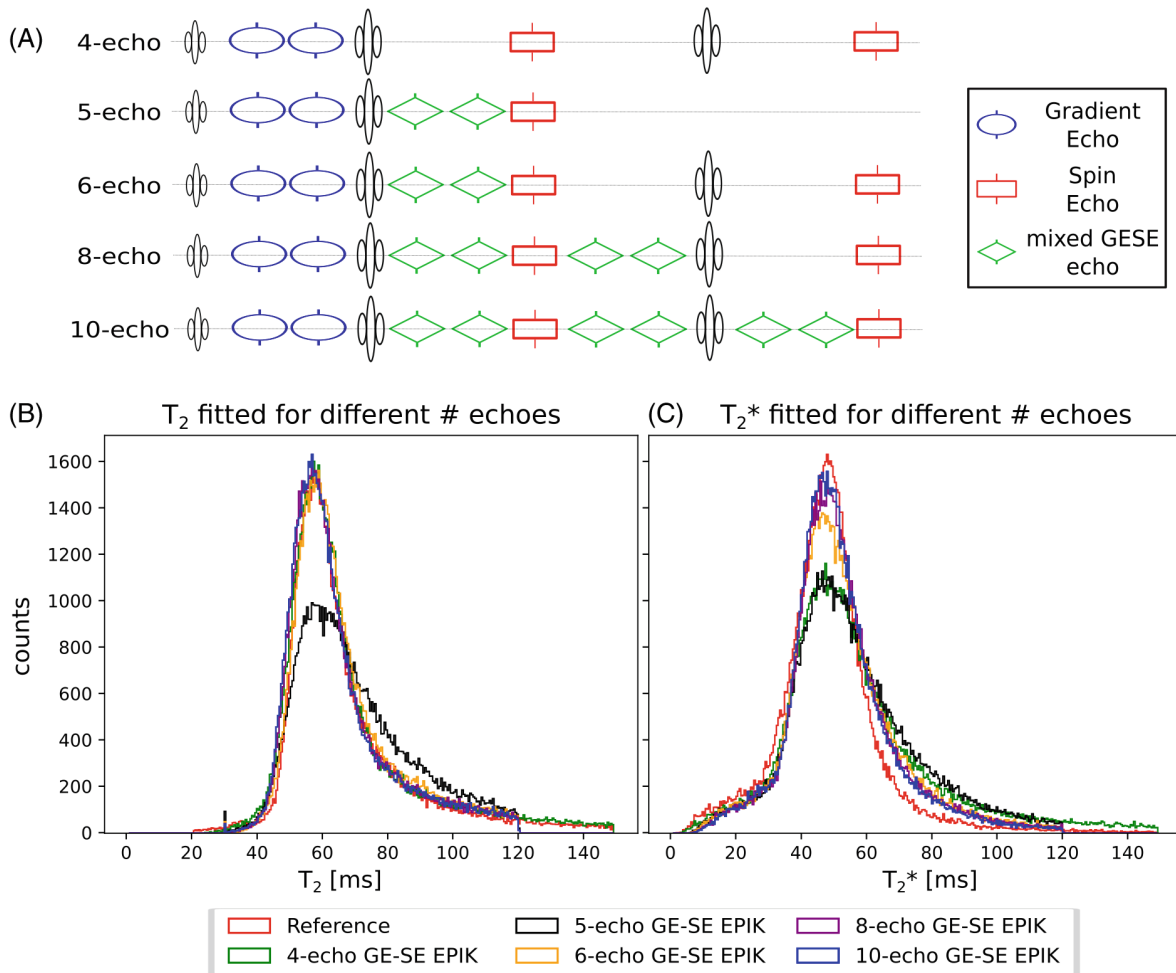


FIGURE 6 Comparison of resulting T_2 (B) and T_2^* (C) distributions based on different numbers of fitted echoes for an in vivo data set. A 10-echo GE-SE EPIK dataset was modified in accordance with the scheme of (A). The mean T_2 value between the five-echo version, including a single SE, and the remaining versions with two SEs, differs by 5.1%, while the variation of mean T_2 in the versions consisting of two SEs is below 1%. The FWHM of the single SE (5-echo) version is 28.6, which reduces to 17.7–18.2 when incorporating a second SE. In terms of T_2^* distributions, the mean value changes by less than 2.1% between the different options, while the FWHM for the 4, 5, 6, 8, 10-echo versions is given by 26.2, 28.1, 23.7, 20.7 and 20.2, respectively. The FWHM of the reference methods is 18.8 for T_2^* and 16.3 for T_2

The mean T_2^* and T_2 values with SD for whole-brain data from all 15 subjects are summarized in Table 1 for the reference and GE-SE EPIK results. The segmented WM and GM values, averaged over all 15 volunteers, are also given and compared to the literature values^{26,27}. Figure 7 shows the distributions of T_2 and T_2^* for the whole brain from all volunteers in the form of 2D histograms to enable a direct comparison between GE-SE EPIK and the respective reference methods; the selected regions from the plots are zoomed and plotted using a log-scale of the voxel number. The mean whole-brain T_2 value from GE-SE EPIK is 58.23 ± 7.31 ms and 59.32 ± 7.42 ms from the sSE reference. Based on the GE-SE EPIK data, the average T_2 is 67.58 ± 5.57 ms for GM, while WM yielded 59.61 ± 6.06 ms. The mean whole-brain T_2^* values from GE-SE EPIK and the mGE reference were found to be 49.76 ± 8.58 ms and 47.79 ± 8.19 ms, respectively. The average T_2^* was

55.14 ± 8.87 ms in GM and 50.32 ± 7.23 ms in WM. All values are summarized in Table 1. Figure 8 presents scatter plots and Bland–Altman plots for the mean T_2 and T_2^* values from the whole population (Figure 8A–D) as well as for representative voxels of a single subject (Figure 8E–H).

3.3 | Oxygen extraction fraction

Oxygen extraction fraction values during a breath-hold experiment consisting of three breath-hold blocks are shown in Figure 9. The time envelope of mean OEF shows a decreasing OEF during breath-hold, followed by recovery during normal breathing. To quantify the OEF changes in the two different states, the slope was fitted by a linear function, where a significant difference between both states is observed (Figure 9C,D).

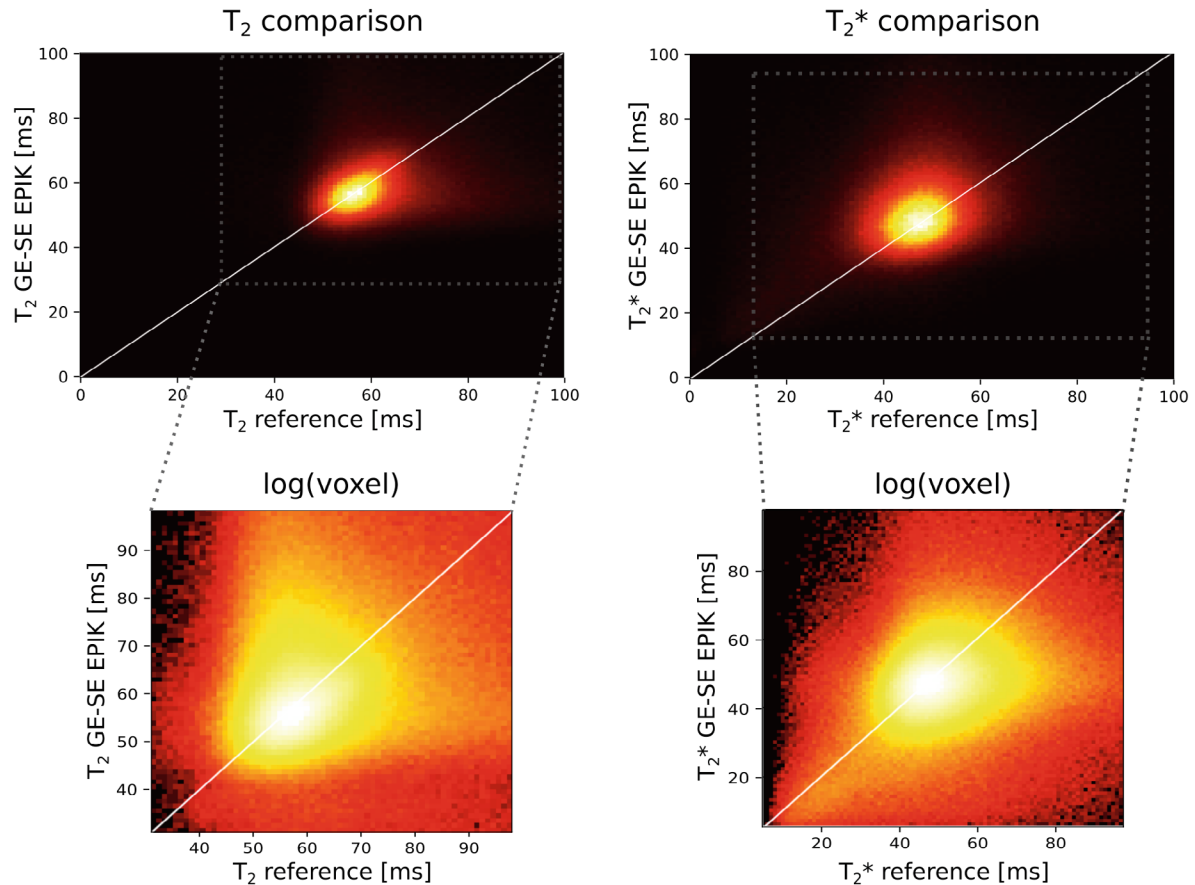


FIGURE 7 2D histogram of T_2 and T_2^* values from 20 slice data for all acquired in vivo subjects and a log-representation of the number of voxels for the zoomed regions

The dynamic OEF time course is plotted together with the corresponding T_2/T_2^* time courses in Figure 9A. OEF maps for two different slices are presented in Figure 9E; the mean OEF value for whole-brain data in the baseline state yields 0.37.

4 | DISCUSSION

4.1 | Relaxometry quantification

Having shown how the inclusion of 10 echoes benefits precision (Figure 4), the results depicted in Figures 5-7 demonstrate that GE-SE EPIK yields mean T_2 and T_2^* values for phantom and in vivo data that are in good agreement with the respective reference methods. A successful spectroscopic validation of T_2^* and T_2 for phantom data was observed. Moreover, in vivo T_2^* results agree with reported literature values at 3T, while the literature covers a broader range for T_2 values, depending on the used method, with those from sSE methods²⁷ matching the GE-SE EPIK values. Despite a longer TA, repeated single SE measurements were chosen as the reference method as

literature results indicate that multi-SE acquisitions, especially CPMG schemes, trend towards an overestimation of T_2 ²⁸ by up to a factor of 1.5²⁹ due to stimulated echo (STE) contributions. Moreover, it has been shown that in a biological system, the expected value of T_2 depends on how it is measured, irrespective of STE contributions, with a well-characterized dependence on the inter-echo spacing. Thus, any comparison with a “gold standard” should aim to match this parameter as closely as possible. Internal consistency between GE-SE EPIK and reference methods was obtained from three phantom acquisitions and a study group of 15 volunteers. As expected, GM/WM segmentation was shown to yield the expected contrast, and the mean WM and GM values obtained from GE-SE EPIK agree well with the literature for T_2 ²⁶ and T_2^* ^{27,30}.

Nevertheless, for an accurate and robust quantification of simultaneous T_2 and T_2^* , several sources of potential errors need to be considered:

A crucial parameter for a successful relaxometry quantification is the refocusing efficiency as a slice profile mismatch was found to effectively diminish the SE signal³¹. However, due to a good agreement between T_2^* and T_2 values from GE-SE EPIK, reference methods and literature,

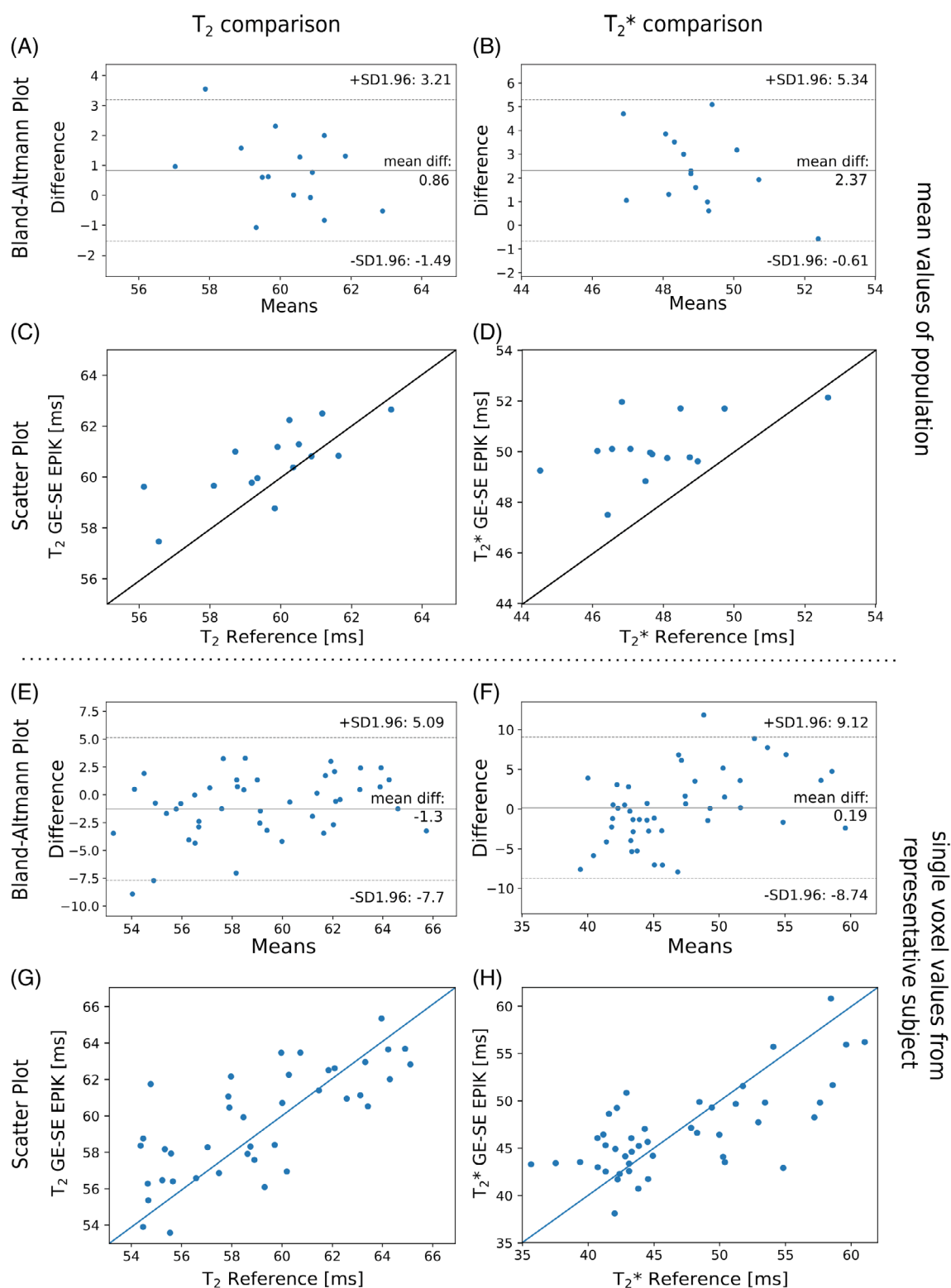


FIGURE 8 Scatter and Bland–Altman plots of the mean T₂ (left column) and T₂* (right column) values from each subject (A–D) and single-voxel T₂/T₂* values of a representative subject data (E–H) areas a comparison between GE-SE EPIK and reference methods

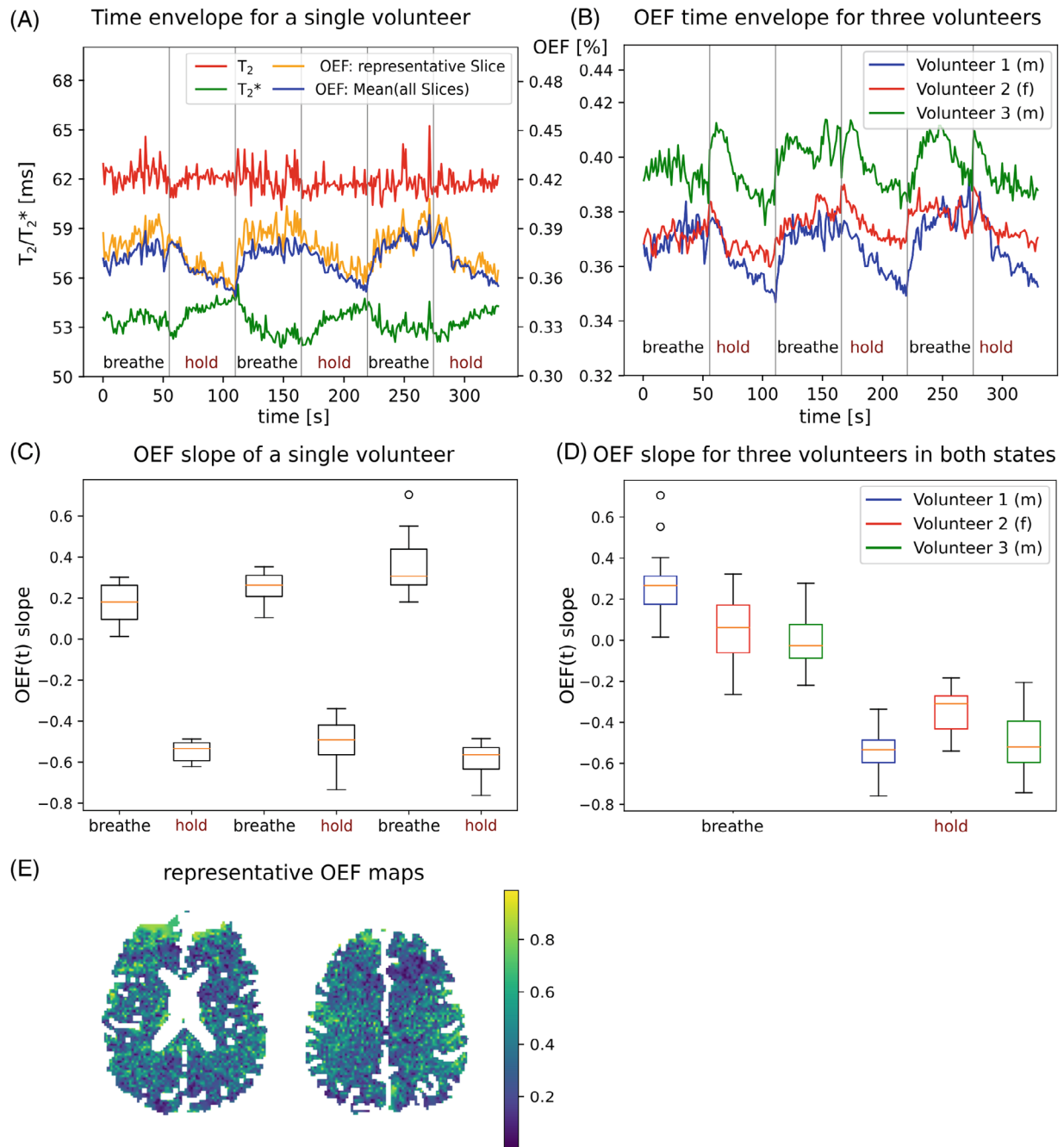


FIGURE 9 Oxygen extraction fraction (OEF) results from breath-hold experiments, including the time course for a single volunteer (A) showing a representative slice as well as the mean OEF from all slices in combination with the dynamic T_2 and T_2^* time course. A boxplot of the respective slopes from each experimental block is given in (C). A comparison between the mean OEF time envelope of three volunteers is shown in (B) with the overall slope of all three normal breathing blocks and the three breath-hold sections being compared for the three volunteers (D). Representative OEF maps for two slice locations are shown in (E)

the described effect is only expected to have a minor or negligible influence. Correction for the effects of B1+ inhomogeneities requires careful consideration. Although B1+ correction was not included here, preliminary results from two randomly selected subjects showed that B1+ inhomogeneities did not significantly influence relaxometry or OEF accuracy – with or without B1+ correction. That is to

say, a difference of less than 0.2% between the mean T_2/T_2^* values of both approaches was found. However, generally, the refocusing efficiency, as well as B1+ inhomogeneities, warrant careful consideration when designing experimental protocols in which comparability and reproducibility with measurements at different scanners or other sites are of importance.

Moreover, partial volume effects, which are more pronounced for larger voxel sizes, require consideration. Although our approach increases the spatial resolution compared to previous GE-SE sequences, thereby reducing partial volume effects, they are not totally eliminated.

Physiological motion may disrupt the steady-state signal, which in turn reduces the MR signal³². However, it is anticipated that the incorporation of motion detection and correction modules such as navigator methods³³ or camera-based systems³⁴ could potentially resolve such issues.

Diffusion effects could lead to a potential signal loss, while susceptibility inhomogeneities could also introduce static field inhomogeneities, which are both expected to be more prominent for in vivo data than in the solid phantoms. In addition, although our method assumes that the pure T_2^* and T_2 signal decays mono-exponentially, intra-voxel inhomogeneities could lead to non-exponential FID decay in certain voxels³⁵, causing T_2^* to be underestimated. For our sequence implementation, partial volume effects and larger dephasing due to the large voxel size were indeed expected, but no significant deviation from mono-exponential decay was observed.

4.2 | OEF application

Based on the successful validation of T_2 and T_2^* values from GE-SE EPIK, OEF values were computed and were found to be in agreement with reported literature values and showed good sensitivity to changes during breath-hold experiments. The following paragraph will outline the difficulties of OEF quantification regarding different available methods such as MR and PET.

OEF baseline results in the literature were reported as 0.35¹⁹ and 0.41³⁶ for MRI methods, while two PET studies reported a mean OEF value of 0.36–0.39³⁷ and 0.44³⁸. The estimated values from our results are in good agreement.

The current gold standard for OEF quantification is O_{15} -PET. While an assessment of the oxygenation information by non-invasive MR techniques is favorable, a direct comparison between both modalities needs careful consideration. An overview of general considerations for MR and PET-based OEF methods can be found in the Supporting Information Appendix S1.4.

The physiological dependencies of OEF results obtained by the approach based on Equation (3), especially the venous blood volume fraction, play an important role and need to be carefully chosen or even experimentally evaluated for individual measurements. In this study, λ was assumed to be constant over the whole breath-hold experiment. In future studies, a direct measure of λ would be beneficial to account for possible changes between

the baseline state and breath-holding. Further limitations of the proposed method lie in the accuracy of R_2' . First, it is known that R_2^* can be diminished by dephasing effects. However, here these were reduced by employing a higher-order shimming (third) prior to each acquisition. Second, partial volume effects lead to CSF inclusion, resulting in an overestimation of R_2' and OEF. Furthermore, while a consistent and optimal choice of the FA, i.e., 90°, would have reduced the likelihood of unintended effects, quantification results from a phantom study show the choice of a reduced FA of 75° is not expected to influence the quantification performance. The underlying model from He et al.²² assumes a random vessel orientation which may be violated in voxels with large vessels. While the linear exponential decay in Equations (1) and (3) is an assumption of the long timescale defined by $1.5 \bullet t_c$ ²², it is noted that the signal contributions from extracellular space and intravascular blood relax quickly. The proposed sequence has an echo spacing of 10 and 20 ms around the SEs, which is in agreement with the critical limit of $1.5 \bullet t_c = 9.4$ –12.5 ms calculated by assuming mean OEF values between 0.37–0.50 a priori.

Overall, it is evident that careful evaluation of the measurement parameters and study settings prior to using either MRI or O_{15} -PET is necessary, as the resulting OEF quantification depends on several factors described above. While the advantages of MRI methods have made them more promising for OEF quantification^{39–41}, only a few methods have been compared directly to PET results. The review from Fan et al.⁴² also underlines a residual bias between PET and MRI OEF, while the physiological state is expected to have a significant influence on absolute OEF values.

OEF is directly related to $CMRO_2$ via Fick's principle ($CMRO_2 = C_a \bullet CBF \bullet OEF$), where C_a can be assumed as the constant arterial oxygen content. Thus, the simultaneous quantification of OEF and CBF, as it is enabled by DSC methods with GE-SE acquisitions¹⁸, can provide an estimation of $CMRO_2$. While absolute OEF maps in resting healthy subjects are largely uniform, CBF and $CMRO_2$ have been observed to show regional variations⁴³. Thus, the direct relation between OEF and CBF offers valuable information about brain metabolism. As the dynamic time course is sensitive to metabolic changes, e.g., decreasing arterial O_2 during long breath-holds, the strength of the OEF slope during breath-hold and the following recovery during normal breathing may reflect the status of brain health and oxygen supply. Its interpretation will become more meaningful when CBV/CBF is directly measured in combination with OEF. The use of Equation (3) for OEF calculation assumes an arterial oxygen saturation (SO_2) of 100%. However, although this holds true under normal conditions, in the scope of clinical evaluations, a direct

measurement of SO_2 , e.g., with a pulse oximeter, is recommended to correct for any possible deviations. Details on the implications of SO_2 on the presented OEF results are given in the Supporting Information Appendix S1.5.

Furthermore, the CBV quantification has been shown to yield higher values in PET measurements compared to MRI. An animal study⁴⁴ compared CBV values from DSC-MRI with O_{15} - CO_2 PET, leading to 2.5 times higher PET values. Thus, MRI may provide different sensitivity to smaller vessels than PET. Moreover, arterial blood volume (CBVa) and blood flow (CBF) measured by arterial spin labeling MRI showed moderate correlation with values derived by O_{15} -PET. MR-derived values were underestimated by 30% and 73%, respectively, in comparison to PET-derived values⁴⁵.

Observing such bias between PET and MRI based OEF/CBV quantification highlights the need for a careful evaluation and interpretation. Future studies will assess both methodologies simultaneously using hybrid PET-MRI. This will reduce scan time and radiation dose while offering a direct comparison for acquisitions of the same physiological state. It is anticipated that the newer generation of hybrid MR-PET hardware will also shed further light on this issue. Moreover, an individual estimation of λ for each volunteer would improve the OEF accuracy and sensitivity.

So far, when comparing absolute OEF values between our method and reported MR and PET literature, good agreement has been observed, and, moreover, a good sensitivity of OEF values was observed for challenge-related changes during breath-hold experiments. The decreasing OEF during breath-hold is explained as the arterial CO_2 increases while arterial O_2 decreases. The increased blood flow during short breath-holds results in increased oxygen delivery to the brain and thus a decrease in OEF⁴⁶.

4.3 | Sequence implementation

The current GE-SE EPIK implementation can be adjusted to accommodate commonly used slice/time configurations for accurately tracking physiological changes (e.g., CBV/OEF). Previously published sequences that claim clinical applicability used a TR between 1 and 2 s with 10–15 slices, while five to seven echoes were acquired with matrix sizes between 64×64 and 96×96 (spatial resolution of 3.8/2.7 mm for a common FOV of 240 mm). Our 10-echo GE-SE EPIK sequence implementation can provide 11 slices with a temporal resolution of 1500 ms and a TA of 32 s for a resolution of $1.9 \times 1.9 \times 3 \text{ mm}^3$. Thus, our method can achieve clinical relevance in terms of temporal resolution while providing improvements in the spatial resolution and the number of acquired echoes with

reasonable low TEs (10/20/37/47/57/67/77/94/104/114 ms) compared to previous methods. Even the first two TEs, attributed to pure GEs, are shorter than most previous published sequences; although the SAGE sequence⁴⁷ delivered shorter TEs (4.9/14 ms), this was achieved at the expense of halved matrix size (64×64) compared to GE-SE EPIK. Further SAGE publications^{2,48} show a shorter first TE (8.3 ms), suffering from lower resolution (96×96 matrix), while the second TE was already larger than that for GE-SE EPIK.

Investigations of higher resolutions will be of interest. Matrix sizes of up to 192×192 are possible by maintaining the same keyhole coverage fraction and number of readout lines per shot of the current implementation to prevent a significant TE increase. However, a larger parallel imaging acceleration and partial Fourier incorporation will become necessary, although an increased readout bandwidth and SNR issues may compromise the image performance. Incorporating a multi-band feature will enable the acquisition of more slices in the same TA. A closer evaluation will be the focus of ongoing work in order to make a sequence available with a resolution of up to 1.25 mm.

5 | CONCLUSIONS

This work introduces a novel 10-echo GE-SE EPIK sequence for the simultaneous quantification of T_2 and T_2^* . The sequence can acquire 20 slices within a minute while also providing information from 10 acquired echoes. The sequence overcomes limitations in resolution and number of echoes with reasonably TEs as reported in previously published sequences based on simultaneous GE and SE acquisition and, importantly, includes a second SE. A matrix size of 128×128 was implemented while maintaining a reasonably low TE for all echoes at 3T. T_2 and T_2^* quantification was validated on phantom and in vivo data by comparison with reference methods, showing good internal consistency. In addition, the T_2 and T_2^* quantification methods agreed well with spectroscopy measurements for three carrageenan phantoms. GM and WM T_2 and T_2^* values match the literature well, and the consistency of the approach was demonstrated in a study on 15 healthy volunteers. OEF computation was performed and showed good sensitivity to challenge related changes between normal breathing and breath-holding in three volunteers.

Having established the benefits of the sequence, our focus is now on its usability in a clinical context as well as on future work to further improve the sequence in terms of resolution and speed. Following further development, the sequence is also expected to be well-suited for use

in brain tumor patients, enabling the identification and characterization of tumor heterogeneity within a minute.

ACKNOWLEDGEMENTS

We thank our colleagues, the MTAs and the organizational team of the INM-4. Special thanks are given to Dennis Thomas and Michael Schöneck for help with the phantom production and Claire Rick for English proofreading.


DATA AVAILABILITY STATEMENT

The original in vivo data can be shared by submitting a request to the corresponding author (N. Jon Shah: n.j.shah@fz-juelich.de) under a formal data-sharing agreement. The sharing is based on the consent of the subject whose data are to be shared; these subjects will be informed beforehand.

ORCID

Fabian Küppers  <https://orcid.org/0000-0002-8365-6931>

Seong Dae Yun  <https://orcid.org/0000-0001-7398-1899>

N. Jon Shah  <https://orcid.org/0000-0002-8151-6169>

REFERENCES

- Schmainda KM, Rand SD, Joseph AM, et al. Characterization of a First-Pass Gradient-Echo Spin-Echo Method to Predict Brain Tumor Grade and Angiogenesis. *AJNR Am J Neuroradiol*. 2004;25:1524-1532.
- Stokes AM, Skinner JT, Quarles CC. Assessment of a combined spin- and gradient-echo (SAGE) DSC-MRI method for preclinical neuroimaging. *Magn Reson Imaging*. 2014;32:1181-1190.
- Boxerman JL, Hamberg LM, Rosen BR, Weisskoff RM. Mr contrast due to intravascular magnetic susceptibility perturbations. *Magn Reson Med*. 1995;34:555-566.
- Yablonskiy DA, Haacke EM. Theory of NMR signal behavior in magnetically inhomogeneous tissues: the static dephasing regime. *Magn Reson Med*. 1994;32:749-763.
- Yamauchi H, Fukuyama H, Nagahama Y, et al. Evidence of misery perfusion and risk for recurrent stroke in major cerebral arterial occlusive diseases from PET. *J Neurol Neurosurg Psychiatry*. 1996;61:18-25.
- Fan AP, Khalil AA, Fiebach JB, et al. Elevated brain oxygen extraction fraction measured by MRI susceptibility relates to perfusion status in acute ischemic stroke. *J Cereb Blood Flow Metab*. 2020;40:539-551.
- Seiler A, Deichmann R, Nöth U, et al. Oxygenation-sensitive magnetic resonance imaging in acute ischemic stroke using T_2'/R_2' mapping: influence of relative cerebral blood volume. *Stroke*. 2017;48:1671-1674.
- Buxton RB. Interpreting oxygenation-based neuroimaging signals: the importance and the challenge of understanding brain oxygen metabolism. *Front Neuroenergetics*. 2010;2:8.
- Manhard MK, Stockmann J, Liao C, et al. A multi-inversion multi-echo spin and gradient echo echo planar imaging sequence with low image distortion for rapid quantitative parameter mapping and synthetic image contrasts. *Magn Reson Med*. 2021;86:866-880.
- Eichner C, Jafari-Khouzani K, Cauley S, et al. Slice accelerated gradient-echo spin-echo dynamic susceptibility contrast imaging with blipped CAIPI for increased slice coverage: slice accelerated GESE DSC. *Magn Reson Med*. 2014;72:770-778.
- Thomas DL, Lythgoe MF, Gadian DG, Ordidge RJ. Rapid simultaneous mapping of T2 and T2* by multiple Acquisition of Spin and Gradient Echoes Using Interleaved Echo Planar Imaging (MASAGE-IEPI). *Neuroimage*. 2002;15:992-1002.
- Shah NJ, Zilles K. Verfahren zur Untersuchung eines Objektes mittels Erfassung des Ortsfrequenzraumes. July 2001. European Patent Office, Patent No. DE 199 62 845 C2: 27.03.03.
- Shah NJ, Zilles K. Imaging Process in the Spatial Frequency Space and Useful for Examining the Properties of Object. August 2004. United States Patent and Trademark Office, Patent No. US6781372B2.
- Zaitsev M, Zilles K, Shah NJ. Shared k-space echo planar imaging with keyhole. *Magn Reson Med*. 2001;45:109-117.
- Zaitsev M, D'Arcy J, Collins DJ, Leach MO, Zilles K, Shah NJ. Dual-contrast echo planar imaging with keyhole: application to dynamic contrast-enhanced perfusion studies. *Phys Med Biol*. 2005;50:4491-4505.
- Yun SD, Reske M, Vahedipour K, Warbrick T, Shah NJ. Parallel imaging acceleration of EPIK for reduced image distortions in fMRI. *Neuroimage*. 2013;73:135-143.
- Yun SD, Shah NJ. Whole-brain high in-plane resolution fMRI using accelerated EPIK for enhanced characterisation of functional areas at 3T. *PLOS One*. 2017;12:e0184759. doi:10.1371/journal.pone.0184759
- Shah NJ, Silva NA, Yun SD. Perfusion weighted imaging using combined gradient/spin echo EPIK: Brain tumour applications in hybrid MR-PET. *Human Brain Mapping*. 2021;42:4144-4154.
- Yin Y, Zhang Y, Gao JH. Dynamic measurement of oxygen extraction fraction using a multiecho asymmetric spin echo (MASE) pulse sequence. *Magn Reson Med*. 2018;80:1118-1124.
- Griswold MA, Jakob PM, Heidemann RM, et al. Generalized autocalibrating partially parallel acquisitions (GRAPPA). *Magn Reson Med*. 2002;47:1202-1210.
- Dierkes T, Neeb H, Shah NJ. Distortion correction in echo-planar imaging and quantitative T2* mapping. *Int Congr Ser*. 2004;1265:181-185.
- He X, Yablonskiy DA. Quantitative BOLD: mapping of human cerebral deoxygenated blood volume and oxygen extraction fraction: default state. *Magn Reson Med*. 2007;57:115-126.
- Lu H, Clingman C, Golay X, van Zijl PCM. Determining the longitudinal relaxation time (T1) of blood at 3.0 tesla. *Magn Reson Med*. 2004;52:679-682.
- Eichling JO, Raichle ME, Grubb RL, Larson KB, Ter-Pogossian MM. In vivo determination of cerebral blood volume with radioactive oxygen-15 in the monkey. *Circ Res*. 1975;37:707-714.
- Spees WM, Yablonskiy DA, Oswood MC, Ackerman JJH. Water proton MR properties of human blood at 1.5 tesla: magnetic susceptibility, T1, T2, T, and non-Lorentzian signal behavior. *Magn Reson Med*. 2001;45:533-542.
- Oros-Peusquens AM, Rossi M, Shah N. Magnetic field dependence of the distribution of NMR relaxation time in the living human brain. *MAGMA*. 2008;21:131-147.
- Gras V, Farrher E, Grinberg F, Shah NJ. Diffusion-weighted DESS protocol optimization for simultaneous mapping of the

- mean diffusivity, proton density and relaxation times at 3 tesla. *Magn Reson Med.* 2017;78:130-141.
28. Petrova MV, Doktorov AB, Lukzen NN. CPMG echo amplitudes with arbitrary refocusing angle: explicit expressions, asymptotic behavior, approximations. *J Magn Reson.* 2011;212:330-343.
 29. Bartha R, Michaeli S, Merkle H, et al. In vivo $^1\text{H}_2\text{O}$ T measurement in the human occipital lobe at 4T and 7T by Carr-Purcell MRI: detection of microscopic susceptibility contrast. *Magn Reson Med.* 2002;47:742-750.
 30. Nöth U, Shrestha M, Schüre JR, Deichmann R. Quantitative in vivo T2 mapping using fast spin echo techniques – a linear correction procedure. *Neuroimage.* 2017;157:476-485.
 31. Schmiedeskamp H, Straka M, Bammer R. Compensation of slice profile mismatch in combined spin- and gradient-echo echo-planar imaging pulse sequences. *Magn Reson Med.* 2012;67:378-388.
 32. O'Halloran R, Aksoy M, Aboussouan E, Peterson E, Van A, Bammer R. Real-time correction of rigid-body-motion-induced phase errors for diffusion-weighted steady state free precession imaging. *Magn Reson Med.* 2015;73:565-576.
 33. Buschbeck RP, Yun SD, Shah NJ. 3D rigid-body motion information from spherical Lissajous navigators at small k-space radii: a proof of concept. *Magn Reson Med.* 2019;82:1462-1470.
 34. Godenschweger F, Kägebein U, Stucht D, et al. Motion correction in MRI of the brain. *Phys Med Biol.* 2016;61:R32-R56.
 35. Dahnke H, Schaeffter T. Limits of detection of SPIO at 3.0 T using T2* relaxometry. *Magn Reson Med.* 2005;53:1202-1206.
 36. Ma Y, Mazerolle EL, Cho J, Sun H, Wang Y, Pike GB. Quantification of brain oxygen extraction fraction using QSM and a hyperoxic challenge. *Magn Reson Med.* 2020;84:3271-3285.
 37. Ibaraki M, Miura S, Shimosegawa E, et al. Quantification of cerebral blood flow and oxygen metabolism with 3-dimensional PET and ^{15}O : validation by comparison with 2-dimensional PET. *J Nucl Med.* 2008;49:50-59.
 38. Ito H, Kanno I, Kato C, et al. Database of normal human cerebral blood flow, cerebral blood volume, cerebral oxygen extraction fraction and cerebral metabolic rate of oxygen measured by positron emission tomography with ^{15}O -labelled carbon dioxide or water, carbon monoxide and oxygen: a multicentre study in Japan. *Eur J Nucl Med Mol Imaging.* 2004;31:635-643.
 39. He X, Zhu M, Yablonskiy DA. Validation of oxygen extraction fraction measurement by qBOLD technique. *Magn Reson Med.* 2008;60:882-888.
 40. Wehrli FW, Fan AP, Rodgers ZB, Englund EK, Langham MC. Susceptibility-based time-resolved whole-organ and regional tissue oximetry. *NMR Biomed.* 2017;30:e3495.
 41. Liu P, Dimitrov I, Andrews T, et al. Multi-site evaluations of a T2-relaxation-under-spin-tagging (TRUST) MRI technique to measure brain oxygenation. *Magn Reson Med.* 2016;75:680-687.
 42. Fan AP, An H, Moradi F, et al. Quantification of brain oxygen extraction and metabolism with ^{15}O -gas PET: a technical review in the era of PET/MRI. *Neuroimage.* 2020;220:117136. doi:10.1016/j.neuroimage.2020.117136
 43. Gusnard DA, Raichle ME. Searching for a baseline: functional imaging and the resting human brain. *Nat Rev Neurosci.* 2001;2:685-694.
 44. Østergaard L, Smith DF, Vestergaard-Poulsen P, et al. Absolute cerebral blood flow and blood volume measured by magnetic resonance imaging bolus tracking: comparison with positron emission tomography values. *J Cereb Blood Flow Metab.* 1998;18:425-432.
 45. Heijtel DFR, Petersen ET, Mutsaerts HJMM, et al. Quantitative agreement between ^{15}O H_2O PET and model free QUASAR MRI-derived cerebral blood flow and arterial blood volume. *NMR Biomed.* 2016;29:519-526.
 46. Sasse SA, Berry RB, Nguyen TK, Light RW, Mahutte CK. Arterial blood gas changes during breath-holding from functional residual capacity. *Chest.* 1996;110:958-964.
 47. Skinner JT, Robison RK, Elder CP, Newton AT, Damon BM, Quarles CC. Evaluation of a multiple spin- and gradient-Echo (SAGE) EPI acquisition with SENSE acceleration: applications for perfusion imaging in and outside the brain. *Magn Reson Imaging.* 2014;32:1171-1180.
 48. Stokes AM, Quarles CC. A simplified spin and gradient echo approach for brain tumor perfusion imaging: SAGE for brain tumor perfusion imaging. *Magn Reson Med.* 2016;75:356-362.
 49. Bernstein MA, King KF, Zhou X. Crusher gradients. *Handbook of MRI Pulse Sequences.* Elsevier LTD; 2014:305-315.

SUPPORTING INFORMATION

Additional supporting information may be found in the online version of the article at the publisher's website.

- S1.** Overview of previously published GE-SE sequences with different applications
- S2.** Parameters of 10-echo GE-SE EPIK sequence with 96×96 matrix size
- S3.** Phantom production
- S4.** General considerations for MR and PET-based OEF methods
- S5.** Implications of arterial oxygen saturation (SO_2) on the quantification of OEF

How to cite this article: Küppers F, Yun SD, Shah NJ. Development of a novel 10-echo multi-contrast sequence based on EPIK to deliver simultaneous quantification of T₂ and T₂ with application to oxygen extraction fraction. *Magn Reson Med.* 2022;88:1608-1623. doi: 10.1002/mrm.29305

WOULD YOU LIKE TO POST AN INFORMAL COMMENT ABOUT THIS PAPER, OR ASK THE AUTHORS A QUESTION ABOUT IT?

If so, please visit <https://mrm.ismrm.org/> and register for our Magn Reson Med Discourse site (registration is free).

The screenshot shows the Magn Reson Med Discourse website. At the top, there is a search bar and a user profile icon. Below the header, there are tabs for 'all categories', 'Categories', 'Latest', and 'Top'. A '+ New Topic' button is also visible. The main content area is divided into two columns. The left column, under the 'Categories' tab, lists various MRM Papers with their respective volumes and dates. The right column, under the 'Latest' tab, shows a list of recent topics, including '[April 2022] Reproducible Research Insights with Jakob Assländer', 'MRM Highlights Magazine - Volume 7', and '[April 2022] Q&A with Jakob Assländer and Daniel Sodickson'. Each topic entry includes a small icon, the title, and the number of replies (0) and the time since the last reply (16d).

Magn Reson Med is currently listing the top 8 downloaded papers from each issue (including Editor's Picks) for comments and questions on the Discourse web site.

However, we are happy to list this or any other papers (please email mrm@ismrm.org to request the posting of any other papers.)

We encourage informal comment and discussion about Magn Reson Med papers on this site. Please note, however, that a formal errata from the authors should still be submitted in the usual way via our Manuscript Central online submission system.